Biophysical Journal
Biophysical Letter

Biophysical Society

Multimodal Measurements of Single-Molecule Dynamics Using FluoRBT

Ivan E. Ivanov,[1,2] Paul Lebel,[2,3] Florian C. Oberstrass,[2] Charles H. Starr,[2,4] Angelica C. Parente,[2,4] Athena Ierokomos,[2,4] and Zev Bryant[2,5,*]

[1]Department of Chemical Engineering, [2]Department of Bioengineering, [3]Department of Applied Physics, [4]Program in Biophysics, and [5]Department of Structural Biology, Stanford University, Stanford, California

ABSTRACT Single-molecule methods provide direct measurements of macromolecular dynamics, but are limited by the number of degrees of freedom that can be followed at one time. High-resolution rotor bead tracking (RBT) measures DNA torque, twist, and extension, and can be used to characterize the structural dynamics of DNA and diverse nucleoprotein complexes. Here, we extend RBT to enable simultaneous monitoring of additional degrees of freedom. Fluorescence-RBT (FluoRBT) combines magnetic tweezers, infrared evanescent scattering, and single-molecule FRET imaging, providing real-time multiparameter measurements of complex molecular processes. We demonstrate the capabilities of FluoRBT by conducting simultaneous measurements of extension and FRET during opening and closing of a DNA hairpin under tension, and by observing simultaneous changes in FRET and torque during a transition between right-handed B-form and left-handed Z-form DNA under controlled supercoiling. We discover unanticipated continuous changes in FRET with applied torque, and also show how FluoRBT can facilitate high-resolution FRET measurements of molecular states, by using a mechanical signal as an independent temporal reference for aligning and averaging noisy fluorescence data. By combining mechanical measurements of global DNA deformations with FRET measurements of local conformational changes, FluoRBT will enable multidimensional investigations of systems ranging from DNA structures to large macromolecular machines.

Dynamic observations of individual molecules have contributed unique insight into biological processes such as macromolecular folding and molecular motor function (1,2). However, whereas the conformational dynamics of biological macromolecules are highly multidimensional, single-molecule measurements project these dynamics onto only a few degrees of freedom—sometimes a single dimension, such as the end-to-end extension of the molecule or the distance between two fluorescent dye labels. Combining different single-molecule techniques in the same assay can leverage their individual strengths and increase the number of observables (3). High-resolution mechanical measurements of extension from optical trapping and magnetic tweezers have been combined with single-molecule fluorescence and FRET to track local conformational transitions or observe changes in composition during binding and unbinding events (4–10). In recent applications, high-resolution optical trapping combined with fluorescence has been used to relate different DNA unwinding modes of the helicase UvrD to its conformation and multimeric composition (11), to observe diffusion of single-stranded DNA binding protein on DNA (12), and to relate the tertiary structure of the thiamine pyrophosphate riboswitch to affinity for its ligand (13). Simultaneous fluorescence and manipulation or particle tracking (5) has also been used to correlate mechanics with conformational changes or nucleotide turnover in both linear (14) and rotary (15,16) molecular motors.

Rotor bead tracking (RBT) is a single-molecule method that can directly monitor two mechanical degrees of freedom at high spatiotemporal resolution (17–19). A micron-sized magnetic bead is typically used to apply forces and torques on a DNA molecule, whereas a separate nanoscale rotor bead attached to the side of the DNA is used as a reporter of DNA angle and extension. In the context of a dynamic nucleoprotein complex, changes in extension can arise from bending, stretching, or sequestering of DNA contour length, whereas changes in angle can result from topoisomerization or from trapped writhe

Submitted June 13, 2017, and accepted for publication November 8, 2017.

*Correspondence: zevry@stanford.edu

Paul Lebel's present address is Chan Zuckerberg Biohub, San Francisco, California.

Florian C. Oberstrass's present address is Ultima Genomics, Inc., Fremont, California.

Editor: Enrique De La Cruz.

https://doi.org/10.1016/j.bpj.2017.11.017

(e.g., due to DNA wrapping) or twist (e.g., due to DNA unwinding) (19). Previously, RBT has been used to study DNA structural dynamics under torque, including DNA melting and the transition between B- and Z-DNA (18–21), and to investigate the mechanochemical cycle of the supercoiling motor DNA gyrase (18,19,22). However, RBT is limited to observing only global DNA structural deformations. Local structural features, such as the locations or domain configurations of Z-DNA or melted bubble regions, cannot be directly distinguished. Enzymes bound to DNA cannot be detected unless they deform the DNA substrate, and protein domain movements leading to changes in DNA topology can only be postulated based on other structural or biochemical data.

Here we introduce Fluorescence-RBT (FluoRBT), which combines RBT and single-molecule fluorescence. We test the capabilities of FluoRBT in experiments that probe conformational changes in DNA, highlighting the ability to simultaneously apply mechanical perturbations, measure DNA extension, twist, and torque, and probe local structural transitions via FRET. FluoRBT is implemented by adapting an instrument configured for evanescent dark field imaging and magnetic tweezers manipulation (18), adding optical paths for simultaneous multiwavelength single-molecule fluorescence measurements (Fig. 1 *a*). For imaging the rotor bead, total internal reflection illumination is achieved by focusing an infrared laser beam at the periphery of the objective back focal plane using a pair of small metallic

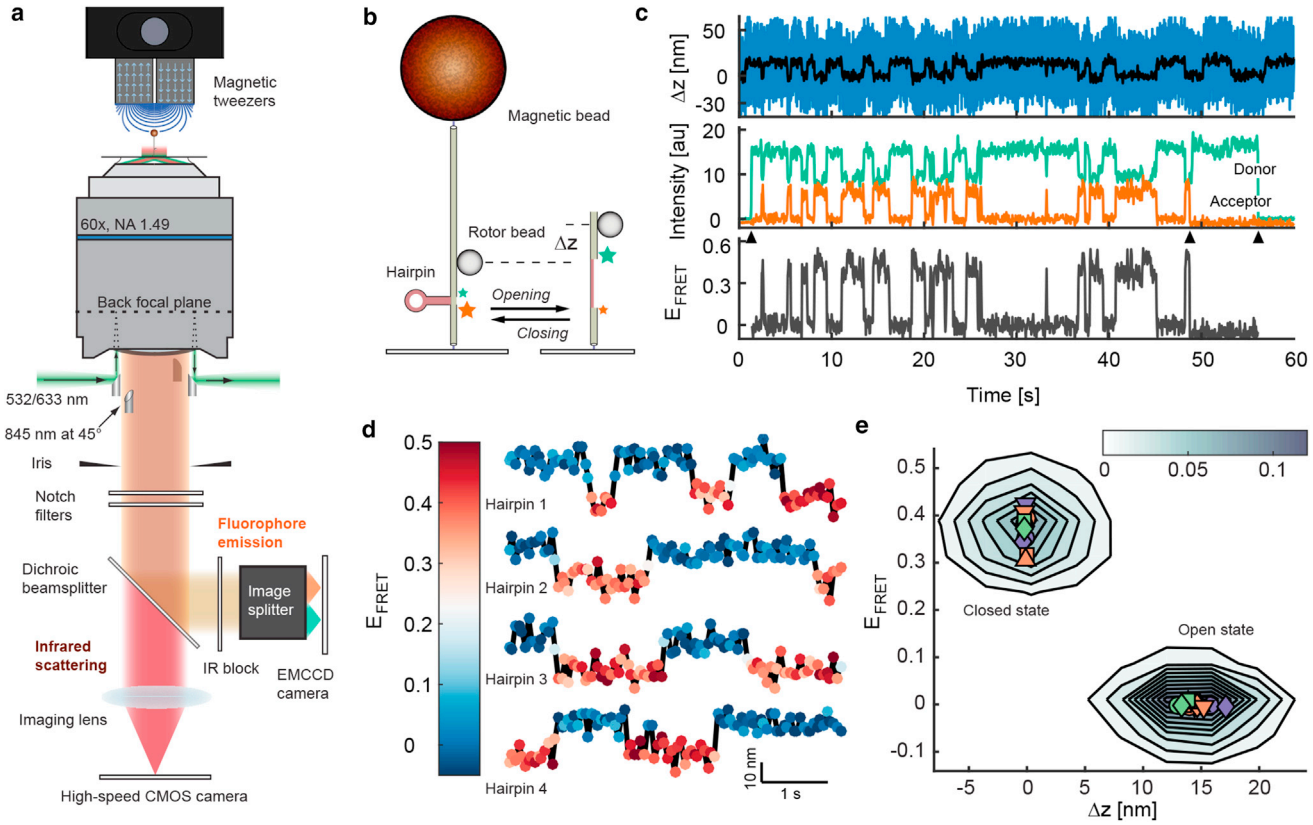

FIGURE 1 **Design and demonstration of combined extension and FRET measurements with FluoRBT. (*a*) A simplified schematic of the experimental setup is shown. Evanescent excitation with 845- and 532-nm light is achieved using a set of small mirrors positioned under the objective. Emitted light is spectrally separated via a dichroic beamsplitter; fluorophore emission is further isolated with a set of optical filters and an IR block. A pair of magnets above the sample is used to apply forces and torques on DNA. See Fig. S1. (*b–e*) Simultaneous measurements of FRET and extension (Δ*z*) were collected during opening and closing of a hairpin under tension. (*b*) A DNA tether was stretched using a magnetic bead, a separate rotor bead was used as an evanescent scattering probe of Δ*z*, and a FRET dye pair (*green star*, Quasar 570; *orange star*, Quasar 670) reported locally on the state of an incorporated hairpin, consisting of 15 basepair stem region and eight nucleotide loop. (*c*) Simultaneously acquired Δ*z* (*top*, 2000 Hz raw and 20 Hz averaged), donor and acceptor intensities (*middle*, 20 Hz), and calculated FRET efficiency (*bottom*) are shown for a single DNA hairpin fluctuating between closed and open states under constant force. Arrowheads show start of donor excitation (~2 s), acceptor bleaching (~48 s), and donor bleaching (~57 s). (*d*) Correspondence between Δ*z* (*vertical axis*) and FRET efficiency (*color scale*) is shown for four separate hairpin tethers. (*e*) Data from 13 hairpin tethers were pooled together to generate a 2D histogram of 6180 instantaneous measurements, presented as a contour plot. Contours are equally spaced; color bar indicates the relative number of observations for each area. The mean Δ*z* extension and FRET efficiency of both states for each molecule are shown with colored symbols. The mean Δ*z* position of the closed state and the mean FRET efficiency of the open state were set to zero in our analysis procedure, as described in Supporting Material.**

mirrors positioned under the objective (18,23). For fluorescence measurements, visible lasers are similarly coupled via a second pair of small mirrors, creating evanescent illumination. The infrared light scattered by the rotor bead is separated from the fluorophore emission using a dichroic beamsplitter. Rotor bead tracking is performed on a fast CMOS camera, and fluorescence is imaged on a sensitive EMCCD camera, after separating light emitted from different fluorophores using an image splitter. Complete methods and technical characterization (Figs. S1–S4) can be found in the Supporting Material.

We first tested the ability of FluoRBT to simultaneously measure extension and FRET during reversible unfolding of a DNA hairpin, a model system that has been employed in prior demonstrations of methods combining the application of force with FRET measurements (9,10). We incorporated a previously characterized hairpin construct (9,24) in the DNA tether, and used both the rotor bead height and a local FRET dye pair to monitor its unfolding (Fig. 1 *b*). Under constant force (~8 pN; see Supporting Materials and Methods in the Supporting Material), we observed concurrent changes in Δz and changes in intensity of the donor and acceptor dyes (Fig. 1, *c* and *d*), reflecting equilibrium fluctuations between the open and closed states of the hairpin. A histogram of data collected from 13 different molecules demonstrates that the instrument resolves the two hairpin states along both extension and FRET efficiency coordinates (Fig. 1 *e*). The measured extension change upon opening of the hairpin is 14.5 ± 1.1 nm, and the FRET efficiency of the closed state is 0.37 ± 0.04 (mean ± SD, $n = 13$ molecules), in agreement with the expected values of ~14 nm and ~0.4, respectively (see Supporting Materials and Methods in the Supporting Material).

An advantage of FluoRBT over other tools that combine extension measurements with fluorescence is that it can also simultaneously measure twist and torque at high resolution (18). RBT has been previously used to observe torque-induced structural transitions in DNA such as duplex melting and Z-DNA formation (18,20,21). In the "static RBT" assay (19), the total twist of the DNA is changed by rotating the magnetic bead, and torque is measured based on the calibrated angular deflection of the DNA segment between the magnetic bead and the rotor bead. Structural transitions in DNA produce characteristic signatures in the torque-twist relationship. As a test of combined FRET and torque spectroscopy, we observed the transition of a GC-repeat sequence of interest (SOI) between right-handed B-form and left-handed Z-form DNA under controlled supercoiling. Torque spectroscopy has previously shown that the B-Z transition of a short GC-repeat sequence displays two-state behavior with a jump in torque at the transition event (21). The B-Z transition has also been observed via single-molecule FRET by incorporating a dye pair in the DNA backbone (7); high salt concentration or negative supercoiling (applied using conventional magnetic tweezers without torque measurement) were found to drive this sequence from a high-FRET state in B-DNA to a low-FRET state in Z-DNA. For FluoRBT measurements, we used a FRET-labeled $d(pGpC)_{11}$ insert, designed based on the construct reported in Lee et al. (7) (Fig. 2 *a*). When we twisted the DNA under 2 pN of tension, we detected the B-Z transition as a jump in torque concurrent with a change in the FRET efficiency of the dye pair incorporated in the DNA backbone (Fig. 2 *b*), consistent with the previous results. Unexpectedly, we also discovered a continuous change in FRET as a function of twist (Fig. 2, *c* and *d*; Figs. S5 and S6), which likely

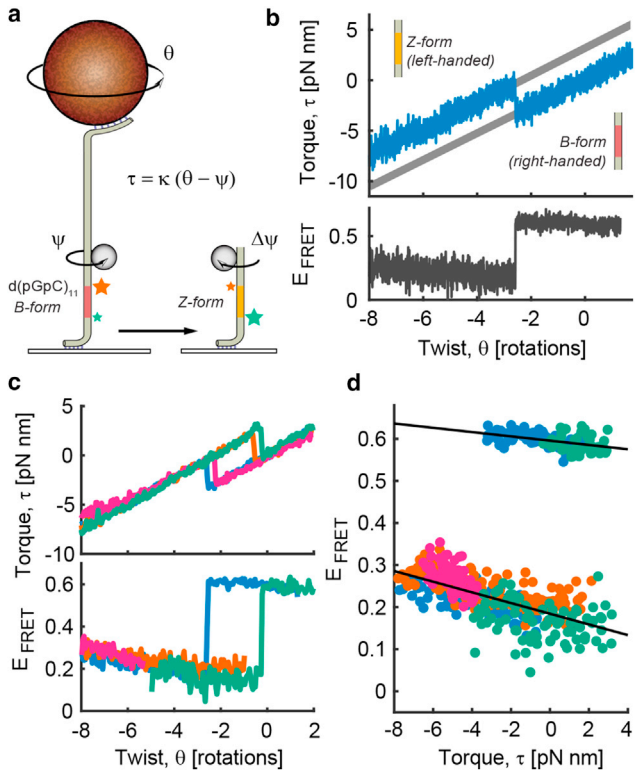

FIGURE 2 **Simultaneous measurements of FRET and torque. (*a*) A GC-repeat sequence was incorporated in a DNA tether. The magnetic bead was rotated to change the total twist (θ) in the DNA while using a rotor bead to measure the torque (τ) and a local FRET pair (*green star*, Cy3; *orange star*, Cy5) to monitor the B-Z structural transition. (*b*) The B-Z transition is observed via simultaneous jumps in torque (*top*, 250 Hz) and FRET efficiency (*bottom*, 5 Hz). Only the rewinding portion of the torque-twist curve is shown. Thick gray lines are fits to torque-twist data before and after the B-Z transition. (*c*) Combined torque and FRET measurements are shown for four different molecules. In the orange and magenta traces, one of the fluorophores bleaches before the structural transition in the SOI is observed. Data are block-averaged in 0.05 rotation (2 s) windows. (*d*) The FRET efficiency shows continuous variation with torque in both the B- and Z-DNA states of the SOI. Trend lines (*black*) were fit to the data from (*c*), after replotting on the torque-FRET plane. FRET changes at a rate of −0.5% $(pN\ nm)^{-1}$ when the SOI is in B-form (*top*) and at a rate of −1.3% $(pN\ nm)^{-1}$ when the SOI is in Z-form (*bottom*).**

reflects compliance in the DNA duplex, particularly in the torsionally soft Z-DNA state. This previously unreported effect (7) may arise from changes in both orientation and separation of the dyes (25) (Fig. S6), and might be exploited to develop molecular torque sensors, analogous to previously described molecular force sensors (26).

Fluorescence is a powerful complement to mechanical measurements as it can report on local structural transitions. However, due to limited photon budgets, single-molecule fluorescence imaging often requires tradeoffs between high signal-to-noise ratio and long observation times (27). In a combined assay, a mechanical signal can in principle provide an independent temporal reference for interpreting fluorescence data, addressing challenges associated with detecting state transitions in noisy FRET traces. Using the DNA hairpin system, we obtained high-resolution FRET measurements of molecular states by averaging fluorescence intensities over many transitions, identified and aligned in time via the extension signal (Fig. 3). We recorded 147 opening transitions in a single molecule, using low fluorescence excitation conditions to extend the observation window at the expense of signal-to-noise ratio (Fig. 3 *a*; Fig. S8). After postsynchronization (28) to transitions in extension, the averaged FRET data (Fig. 3 *b*) show two well-resolved states of the hairpin, as expected (9,24). When applied to systems that visit multiple states during a single mechanical step, this approach may also reveal short-lived structural intermediates as transients in the averaged FRET data.

FluoRBT expands the toolbox of fluorescence-enabled force spectroscopy techniques by providing the capability to measure FRET simultaneously with DNA torque, twist, and extension. This capability complements tools that apply forces and exclusively measure FRET (9,29), or combine the measurement of fluorescence intensity

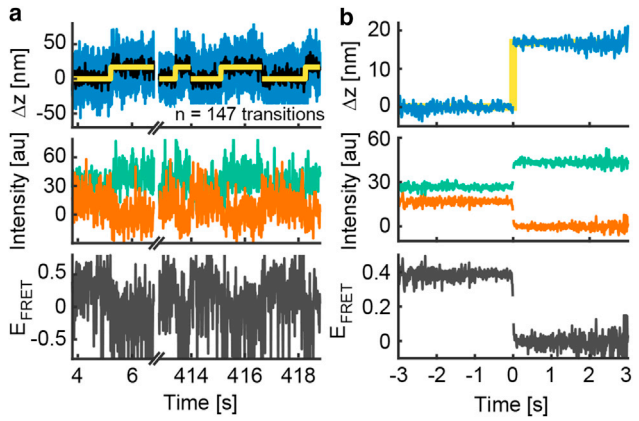

FIGURE 3 High-resolution FRET measurements of molecular states by postsynchronization of fluorescence data to mechanical measurements. DNA hairpin state transitions (*yellow* step function) were assigned based on the Δ*z* signal; data from (*a*) were excised, aligned in time to the opening event, and averaged to generate (*b*). Fluorescence intensity is acquired at 100 Hz. See Fig. S8 for full data trace and further analysis.

(6,8,30) or FRET (7,10–13) with extension alone. The use of magnetic tweezers provides constant force without the need for feedback, and may allow the technique to be extended for parallel measurements on multiple molecules. Alternative methods for measuring torque and twist (19,31–33) could in principle also be combined with single-molecule fluorescence, but do not provide the high spatiotemporal resolution in torque and twist achieved by RBT (18,19,31). FluoRBT may further be extended for imaging of more than two fluorophores and for multicolor FRET, facilitated by the spatial separation of the fluorescence excitation and emission paths (23). The combination of high-speed evanescent dark field tracking (34) with FRET implemented here can also be adapted for investigations of diverse molecular machines, including cytoskeletal motors and rotary ATPases (16). In future applications, FluoRBT may be used to conduct detailed multiparameter studies of DNA structures under torque, and to map the structural conformations of nucleoprotein machines such as gyrase (18,22) or RNA polymerase (35–37) during active cycling through functional states, where well-defined mechanical transitions could be used to temporally align FRET signals repeated using multiple dye pairs, placing constraints on modeling (38) dynamically interconverting molecular architectures.

SUPPORTING MATERIAL

Supporting Materials and Methods, eight figures, two tables, one movie, and one data file are available at http://www.biophysj.org/biophysj/supplemental/S0006-3495(17)31246-8.

AUTHOR CONTRIBUTIONS

I.E.I., P.L., F.C.O., and Z.B. designed research. I.E.I., P.L., F.C.O, and A.I. performed research. C.H.S. and A.C.P. contributed modeling and analytic tools. I.E.I. analyzed data. Z.B. supervised research. I.E.I. and Z.B. wrote the manuscript with input from all authors.

ACKNOWLEDGMENTS

This work was supported by a Tusher Family Stanford Interdisciplinary Graduate Fellowship to I.E.I. and by a National Institutes of Health grant GM106159 to Z.B.

SUPPORTING CITATIONS

References (39–47) appear in the Supporting Material.

REFERENCES

1. Dulin, D., J. Lipfert, …, N. H. Dekker. 2013. Studying genomic processes at the single-molecule level: introducing the tools and applications. *Nat. Rev. Genet.* 14:9–22.
2. Fazal, F. M., and S. M. Block. 2011. Optical tweezers study life under tension. *Nat. Photonics.* 5:318–321.
3. Ha, T. 2014. Single-molecule methods leap ahead. *Nat. Methods.* 11:1015–1018.

4. Gross, P., G. Farge, …, G. J. L. Wuite. 2010. Combining optical tweezers, single-molecule fluorescence microscopy, and microfluidics for studies of DNA-protein interactions. *In* Methods in Enzymology. N. G. Walter, ed. Academic Press, Cambridge, MA, pp. 427–453.
5. Cordova, J. C., D. K. Das, …, M. J. Lang. 2014. Combining single-molecule manipulation and single-molecule detection. *Curr. Opin. Struct. Biol.* 28:142–148.
6. Lang, M. J., P. M. Fordyce, …, S. M. Block. 2004. Simultaneous, coincident optical trapping and single-molecule fluorescence. *Nat. Methods.* 1:133–139.
7. Lee, M., S. H. Kim, and S. C. Hong. 2010. Minute negative superhelicity is sufficient to induce the B-Z transition in the presence of low tension. *Proc. Natl. Acad. Sci. USA.* 107:4985–4990.
8. Comstock, M. J., T. Ha, and Y. R. Chemla. 2011. Ultrahigh-resolution optical trap with single-fluorophore sensitivity. *Nat. Methods.* 8:335–340.
9. Long, X., J. W. Parks, …, M. D. Stone. 2013. Mechanical unfolding of human telomere G-quadruplex DNA probed by integrated fluorescence and magnetic tweezers spectroscopy. *Nucleic Acids Res.* 41:2746–2755.
10. Kemmerich, F. E., M. Swoboda, …, M. Schlierf. 2016. Simultaneous single-molecule force and fluorescence sampling of DNA nanostructure conformations using magnetic tweezers. *Nano Lett.* 16:381–386.
11. Comstock, M. J., K. D. Whitley, …, Y. R. Chemla. 2015. Protein structure. Direct observation of structure-function relationship in a nucleic acid-processing enzyme. *Science.* 348:352–354.
12. Suksombat, S., R. Khafizov, …, Y. R. Chemla. 2015. Structural dynamics of *E. coli* single-stranded DNA binding protein reveal DNA wrapping and unwrapping pathways. *eLife.* 4:e08193.
13. Duesterberg, V. K., I. T. Fischer-Hwang, …, S. M. Block. 2015. Observation of long-range tertiary interactions during ligand binding by the TPP riboswitch aptamer. *eLife.* 4:e12362.
14. Ishijima, A., H. Kojima, …, T. Yanagida. 1998. Simultaneous observation of individual ATPase and mechanical events by a single myosin molecule during interaction with actin. *Cell.* 92:161–171.
15. Adachi, K., K. Oiwa, …, K. Kinosita, Jr. 2007. Coupling of rotation and catalysis in F(1)-ATPase revealed by single-molecule imaging and manipulation. *Cell.* 130:309–321.
16. Sugawa, M., K. Okazaki, …, T. Nishizaka. 2016. F1-ATPase conformational cycle from simultaneous single-molecule FRET and rotation measurements. *Proc. Natl. Acad. Sci. USA.* 113:E2916–E2924.
17. Bryant, Z., M. D. Stone, …, C. Bustamante. 2003. Structural transitions and elasticity from torque measurements on DNA. *Nature.* 424:338–341.
18. Lebel, P., A. Basu, …, Z. Bryant. 2014. Gold rotor bead tracking for high-speed measurements of DNA twist, torque and extension. *Nat. Methods.* 11:456–462.
19. Bryant, Z., F. C. Oberstrass, and A. Basu. 2012. Recent developments in single-molecule DNA mechanics. *Curr. Opin. Struct. Biol.* 22:304–312.
20. Oberstrass, F. C., L. E. Fernandes, …, Z. Bryant. 2013. Torque spectroscopy of DNA: base-pair stability, boundary effects, backbending, and breathing dynamics. *Phys. Rev. Lett.* 110:178103.
21. Oberstrass, F. C., L. E. Fernandes, and Z. Bryant. 2012. Torque measurements reveal sequence-specific cooperative transitions in supercoiled DNA. *Proc. Natl. Acad. Sci. USA.* 109:6106–6111.
22. Basu, A., A. C. Parente, and Z. Bryant. 2016. Structural dynamics and mechanochemical coupling in DNA gyrase. *J. Mol. Biol.* 428:1833–1845.
23. Friedman, L. J., J. Chung, and J. Gelles. 2006. Viewing dynamic assembly of molecular complexes by multi-wavelength single-molecule fluorescence. *Biophys. J.* 91:1023–1031.
24. Woodside, M. T., W. M. Behnke-Parks, …, S. M. Block. 2006. Nanomechanical measurements of the sequence-dependent folding landscapes of single nucleic acid hairpins. *Proc. Natl. Acad. Sci. USA.* 103:6190–6195.
25. Sindbert, S., S. Kalinin, …, C. A. M. Seidel. 2011. Accurate distance determination of nucleic acids via Förster resonance energy transfer: implications of dye linker length and rigidity. *J. Am. Chem. Soc.* 133:2463–2480.
26. Grashoff, C., B. D. Hoffman, …, M. A. Schwartz. 2010. Measuring mechanical tension across vinculin reveals regulation of focal adhesion dynamics. *Nature.* 466:263–266.
27. Roy, R., S. Hohng, and T. Ha. 2008. A practical guide to single-molecule FRET. *Nat. Methods.* 5:507–516.
28. Petrov, A., J. Chen, …, J. D. Puglisi. 2012. Single-molecule analysis of translational dynamics. *Cold Spring Harb. Perspect. Biol.* 4:a011551.
29. Hohng, S., R. Zhou, …, T. Ha. 2007. Fluorescence-force spectroscopy maps two-dimensional reaction landscape of the Holliday junction. *Science.* 318:279–283.
30. Whitley, K. D., M. J. Comstock, and Y. R. Chemla. 2017. Elasticity of the transition state for oligonucleotide hybridization. *Nucleic Acids Res.* 45:547–555.
31. Lipfert, J., J. W. J. Kerssemakers, …, N. H. Dekker. 2010. Magnetic torque tweezers: measuring torsional stiffness in DNA and RecA-DNA filaments. *Nat. Methods.* 7:977–980.
32. Lipfert, J., M. Wiggin, …, N. H. Dekker. 2011. Freely orbiting magnetic tweezers to directly monitor changes in the twist of nucleic acids. *Nat. Commun.* 2:439.
33. La Porta, A., and M. D. Wang. 2004. Optical torque wrench: angular trapping, rotation, and torque detection of quartz microparticles. *Phys. Rev. Lett.* 92:190801.
34. Isojima, H., R. Iino, …, M. Tomishige. 2016. Direct observation of intermediate states during the stepping motion of kinesin-1. *Nat. Chem. Biol.* 12:290–297.
35. Abbondanzieri, E. A., W. J. Greenleaf, …, S. M. Block. 2005. Direct observation of base-pair stepping by RNA polymerase. *Nature.* 438:460–465.
36. Ma, J., L. Bai, and M. D. Wang. 2013. Transcription under torsion. *Science.* 340:1580–1583.
37. Chakraborty, A., D. Wang, …, R. H. Ebright. 2012. Opening and closing of the bacterial RNA polymerase clamp. *Science.* 337:591–595.
38. Choi, U. B., P. Strop, …, K. R. Weninger. 2010. Single-molecule FRET-derived model of the synaptotagmin 1-SNARE fusion complex. *Nat. Struct. Mol. Biol.* 17:318–324.
39. Kalinin, S., T. Peulen, …, C. A. M. Seidel. 2012. A toolkit and benchmark study for FRET-restrained high-precision structural modeling. *Nat. Methods.* 9:1218–1225.
40. Nishizaka, T., Y. Hasimoto, and T. Masaike. 2011. Simultaneous observation of chemomechanical coupling of a molecular motor. *In* Single Molecule Enzymology: Methods and Protocols.. G. I. Mashanov and C. Batters, eds. Humana Press, Totowa, NJ, pp. 259–271.
41. Sarkar, A., R. B. Robertson, and J. M. Fernandez. 2004. Simultaneous atomic force microscope and fluorescence measurements of protein unfolding using a calibrated evanescent wave. *Proc. Natl. Acad. Sci. USA.* 101:12882–12886.
42. Watanabe, T. M., T. Sato, …, H. Higuchi. 2007. Three-dimensional nanometry of vesicle transport in living cells using dual-focus imaging optics. *Biochem. Biophys. Res. Commun.* 359:1–7.
43. Milescu, L. S., C. Nicolai, and J. Bannen. 2000–2013. QuB Software.
44. Huguet, J. M., C. V. Bizarro, …, F. Ritort. 2010. Single-molecule derivation of salt dependent base-pair free energies in DNA. *Proc. Natl. Acad. Sci. USA.* 107:15431–15436.
45. Zheng, G., X.-J. Lu, and W. K. Olson. 2009. Web 3DNA—a web server for the analysis, reconstruction, and visualization of three-dimensional nucleic-acid structures. *Nucleic Acids Res.* 37:W240–W246.
46. Stein, I. H., V. Schüller, …, T. Liedl. 2011. Single-molecule FRET ruler based on rigid DNA origami blocks. *ChemPhysChem.* 12:689–695.
47. Woźniak, A. K., G. F. Schröder, …, F. Oesterhelt. 2008. Single-molecule FRET measures bends and kinks in DNA. *Proc. Natl. Acad. Sci. USA.* 105:18337–18342.

Biophysical Journal, Volume *114*

Supplemental Information

Multimodal Measurements of Single-Molecule Dynamics Using FluoRBT

Ivan E. Ivanov, Paul Lebel, Florian C. Oberstrass, Charles H. Starr, Angelica C. Parente, Athena Ierokomos, and Zev Bryant

Supporting Material

Table of Contents

Methods

Instrumentation. Experiments were performed on a custom-built evanescent darkfield microscope, as previously described (1). The instrument was modified for fluorescence microscopy by constructing an additional optical path for excitation with 532 nm and 633 nm light (Fig. S1). In the experiments described here, fluorophores were excited with only 532 nm light. Rotor bead scattering was imaged on a CMOS camera (Mikrotron EoSens CL) at 2000 Hz for hairpin opening experiments (Fig. 1 and Fig. 3), and at 250 Hz for studying the B-Z DNA transition (Fig. 2). Fluorophore emission was imaged on an EMCCD camera (Andor iXon+ 897) at 100 Hz for postsynchronization experiments, at 20 Hz for hairpin opening experiments, and at 5 Hz for studying the B-Z DNA transition. Acquisition from the two cameras was synchronized via TTL triggers (Fig. S3). Brightfield imaging of the magnetic bead was not performed simultaneously with fluorescence and scattering measurements, but was used separately for force calibration as in previous work (1), and for approximate spatial alignment of the two cameras. Focus stabilization (1) was run at 4 Hz after choosing the focal plane that minimizes coupling between the evanescent nanometry signal and the z-motion of the microscope stage (see Supplementary Figure 9 in Ref. (1)). Hairpin opening experiments were performed under ~8 pN of tension, such that the open and closed states were approximately equally probable.

Fluorescence illumination conditions. We used sample irradiance of ~500 W/cm^2 for typical hairpin opening experiments (Fig. 1), and ~50 W/cm^2 for studying the B-Z DNA transition (Fig. 2) and for postsynchronizing fluorescence data to mechanical data (Fig. 3). We used approximately s-polarized fluorescence excitation light for all experiments (Fig. S1), and fluorophore intensities can depend on dipole orientation. Switching to circular polarization in the excitation beam only partially alleviates anisotropic effects in typical TIRF illumination geometries, although alternative designs have been developed to achieve near-isotropic excitation (2). In hairpin opening experiments shown here, dye attachment via flexible linkers (see Note 1 and Table S2) is expected to allow orientational averaging through rapid rotation of the dyes (3). In the d(pGpC)$_{11}$ construct, fluorescent dyes are incorporated into the DNA backbone and may experience restrained rotational mobility (refer to Fig. S6). In FRET experiments, the relative orientation of the donor dipole with respect to the

polarization axis may influence the recorded signal intensity, but the measured FRET efficiency is largely unaffected, as it depends on the ratio of the donor and acceptor intensities.

DNA tether design. DNA tethers were constructed by ligation of restriction enzyme digested PCR products, as previously described (1,4,5). The DNA hairpin and the $d(pGpC)_{11}$ sequence of interest were constructed from hybridized synthetic oligonucleotides; both sequences were adapted from model systems previously reported in the literature (6-8). The hairpin construct used in all experiments described here was 15R60/T8, with the exception of data presented in Figure S4b where 20R60/T4 was used. See Note 1 for details.

Sample preparation. Imaging was performed in fluidic chambers, as described before (1). Rotor beads used in these experiments were 300 nm Power-Bind streptavidin coated polystyrene particles (Thermo Fisher Scientific, 29000701011150). Hairpin opening experiments were performed in 20 mM Tris-HCl pH 8.0, 10 mM NaCl, 1 mM EDTA, 0.2% Tween-20, 0.2 mg/ml BSA, 0.01% NaN_3, and 1x oxygen scavenging reagents (0.4% glucose, 1250 U/ml glucose oxidase (Sigma-Aldrich, G2133), 100 000 U/ml catalase (Sigma-Aldrich, C100), and ~2 mM Trolox (Sigma-Aldrich, 238813)). Torque-twist curves were performed in 40 mM Tris-HCl pH 8.0, 100 mM NaCl, 5 mM EDTA, 0.2% Tween-20, 0.2 mg/ml BSA, 0.01% NaN_3, and 1x oxygen scavenging reagents.

Torque spectroscopy. Torque-twist curves (Fig. 2) were collected under 2 pN of tension. The total twist of the molecule was changed at 9°/s by rotating the magnetic tweezers. Twist was ramped from 0 rotations to -10 rotations during the unwinding phase, and then from -10 rotations to +2 rotations during the rewinding phase of the torque-twist curve. Torque was calculated based on the angular deflection of the calibrated transducer segment between the magnetic bead and the rotor bead, i.e. $\tau = \kappa\,\alpha$, where $\kappa = 0.26\,pN\,nm/rad$ is the torsional stiffness of the transducer, and $\alpha = \theta - \psi$ is the difference in angle between the magnetic bead (θ) and the rotor bead (ψ). The angle of the magnetic tweezers corresponding to $\theta = 0$ was set by maximizing the extension of the DNA tether under low force (4,5). Fluorescence excitation was turned on only for part of the rewinding cycle, due to the limited observation lifetime of the fluorophores.

Data analysis. Rotor bead tracking was performed as previously described (1). Briefly, the angle of the rotor bead was calculated from its x-y trajectory, and Δz was determined from the intensity of the rotor bead in the

evanescent field using $\Delta z = -\Lambda \log(I/I_0)$, where I_0 is the intensity at a reference z height, and Λ is the evanescent field delay length (9). As described in detail previously (1), Λ was determined by collecting *z* fluctuations and cross-calibrating with dual-focus imaging (1,10), after calibrating the dual-focus method by stepping the piezo stage. For the experiments reported here, we used $\Lambda = 210$ nm, based on averaging calibrations obtained for individual molecules.

Extension and torque data were block-averaged in bins matching the acquisition rate of the fluorescence signal. Extension data from hairpin unfolding experiments were assigned to the open or closed states by fitting the time traces to a two-state hidden Markov model (HMM) using the segmental k-means method in QuB (11). The extension at the peak of the Gaussian function fit to the closed state in each trace was set to $\Delta z = 0$.

Recorded intensity in the donor and acceptor channels was corrected for fluorescence background and for weak constant signal that sometimes arose from infrared excitation of the magnetic bead. Acceptor intensity was further corrected for spectral cross-talk from the donor channel and for direct excitation from the donor excitation source. The γ factor, accounting for differences in quantum yield and detection efficiency between the two fluorophores, was calculated from changes in donor and acceptor intensity during hairpin opening or at the acceptor photobleaching event. FRET efficiency was calculated from $E_{FRET} = \left(1 + \gamma \, {I_D}/{I_A}\right)^{-1}$, where I_D and I_A are, respectively, the corrected donor and acceptor intensities (12). Correction factors were calculated for each individual molecule when possible; otherwise average values from ensemble measurements were used. We defined $I_A = 0$ in the open hairpin state due to the large spatial separation between the two dyes.

Data selection. We followed DNA tether selection criteria as described in Lebel et al. (1), except that rotor beads showing unconstrained angular fluctuations were selected for DNA hairpin tethers, consistent with the design. We verified that the hairpin construct showed reversible transitions in Δz before collecting FluoRBT measurements. For hairpin opening experiments, we collected data on 35 DNA tethers. Of those, 8 were missing a donor or an acceptor dye, 10 produced fluorescence traces shorter than 10 seconds, 2 showed low SNR, and 2 showed anomalous very slow or absent FRET transitions. In Figure 1 we report on the remaining 13 molecules. For studying the B-Z DNA transition, we collected data on 25 DNA tethers. Of those, 6 were missing a donor or an acceptor dye, 7 did not show two-state torque-twist curves, 2 showed rare intermediates

in E_{FRET} (see Fig. S7), and 2 showed short or blinking fluorescence traces. We report on the remaining 8 molecules in Figures 2, S5, and S6.

Structural modeling. The predicted hairpin opening distance for 15R60/T8 was calculated as the difference in extension of the 38 bases of single-stranded DNA of the hairpin in the open state (16.0 nm at 8 pN, based on the Wormlike Chain Model, using parameters d = 0.665 nm/base and l_p = 1.14 nm, as given in (13)) and the 2 nm width of double-stranded DNA helix of the hairpin in the closed state, giving a predicted Δz = 14.0 nm.

The expected FRET efficiency in the closed hairpin state was determined by modeling the position of the donor and the acceptor. The dyes are attached to thymidine bases via flexible linkers, allowing for rotational mobility, and the DNA segments above and below the hairpin can swivel relative to each other (see Note 1 and Table S2). The mean dye position on 3-HNDL and 5-HNDL was derived from accessible volume (AV) calculations (3) using duplex models generated in Web 3DNA (14), linker lengths of 20 Å for the donor and 22 Å for the acceptor, linker width of 4.5 Å, and dye radius of 3.5 Å. In the calculated mean positions, the donor and the acceptor are radially displaced from the central axis of DNA by 12.0 Å and 11.5 Å, respectively. The axial separation between the dyes was calculated as 48 Å, after including 28 Å of separation between the duplex models to account for the intervening closed DNA hairpin and flanking abasic sites (see Note 1 and Table S2). Using R_0 = 53 Å (15), isotropic averaging (16) over swiveling motions then yields E_{FRET} = 0.42 for the closed state of the hairpin. In the open state of the hairpin, the fluorophores are much more than two Förster radii apart (~20 nm separation). We have defined $E_{FRET} = 0$ in the open hairpin state (see above), and thus cannot determine the hairpin opening distance from FRET data.

To model the approximate donor and acceptor dye positions on the $d(pGpC)_{11}$ DNA helix for the geometric calculations shown in Figure S6, we generated B-DNA and Z-DNA helices using Web 3DNA (14) and then simulated average dye positions in Crystallography and NMR System (CNS) by adapting a torsion angle molecular dynamics approach described earlier (17), holding the DNA fixed while allowing dyes and linkers to fluctuate. 500 simulated annealing trials were run for each DNA model, and average dye positions were calculated based on the position of the central dye carbon in the polymethine bridge.

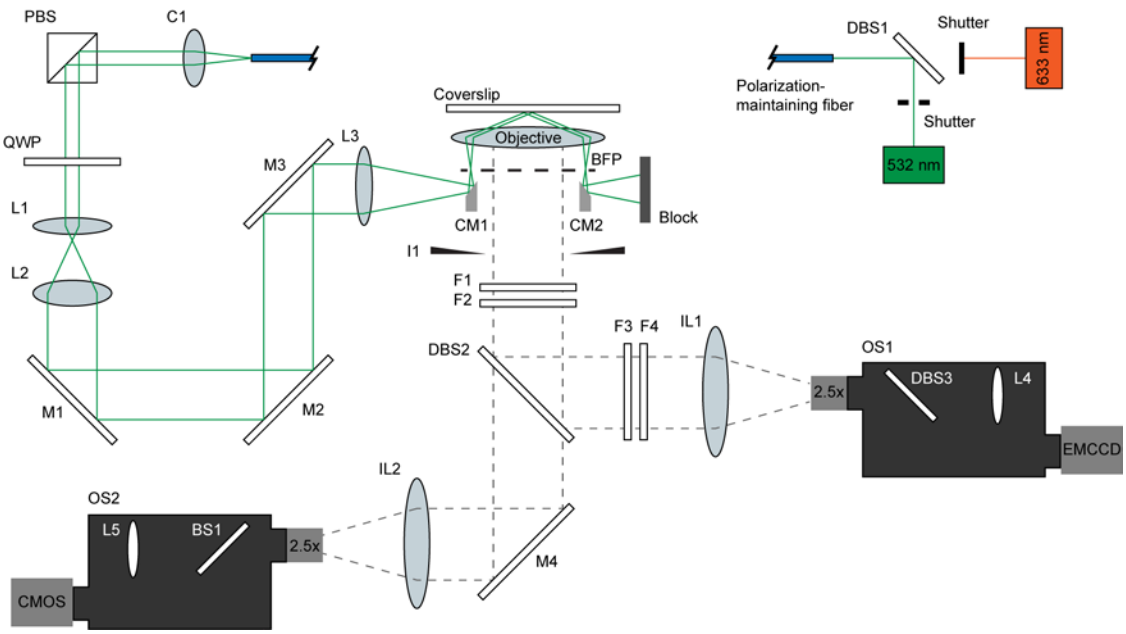

Figure S1. Optical schematic of fluorescence excitation and emission paths. Light from 532 nm and 633 nm lasers was coupled into a polarization-maintaining fiber. The beam at the fiber exit was collimated (C1), expanded (using lenses L1 and L2, achieving ~1500 μm^2 spot at the sample), and then focused onto the objective back focal plane (BFP) via an achromatic lens (L3) and a small metallic coupling mirror (CM1). A polarizing beam splitter (PBS) and quarter-wave plate (QWP) allow adjusting the polarization of the excitation beam. This work used approximately s-polarized excitation light, as described in Methods. Two notch filters and an iris (F1, F2, and I1) were placed in the emission path to reject stray light. Fluorophore emission was spectrally separated from the longer-wavelength rotor bead scattering using a dichroic beamsplitter (DBS2). Light emitted from the dyes used in these experiments was further isolated using a 550 nm long-pass filter (F3) and 842 nm short-pass filter (F4) and then imaged through an optical splitter (OS1) onto an EMCCD camera. Emission from the donor and acceptor dyes was separated using a dichroic beamsplitter (DBS3) inserted in OS1; a weak lens (L4) was used to reduce the small focal shift between the two channels. Rotor bead scattering was also imaged through an optical splitter (OS2) onto a CMOS camera. A 50/50 beamsplitter (BS1) and a lens (L5) were inserted in OS2 during calibration of the infrared evanescent wave decay length (see Methods and Supplementary Figure 3 in Ref. (1)). Brightfield illumination of the magnetic bead (not shown) was accomplished as described earlier (see Supplementary Figure 1 in Ref (1)). For a complete list of parts, see Note 2.

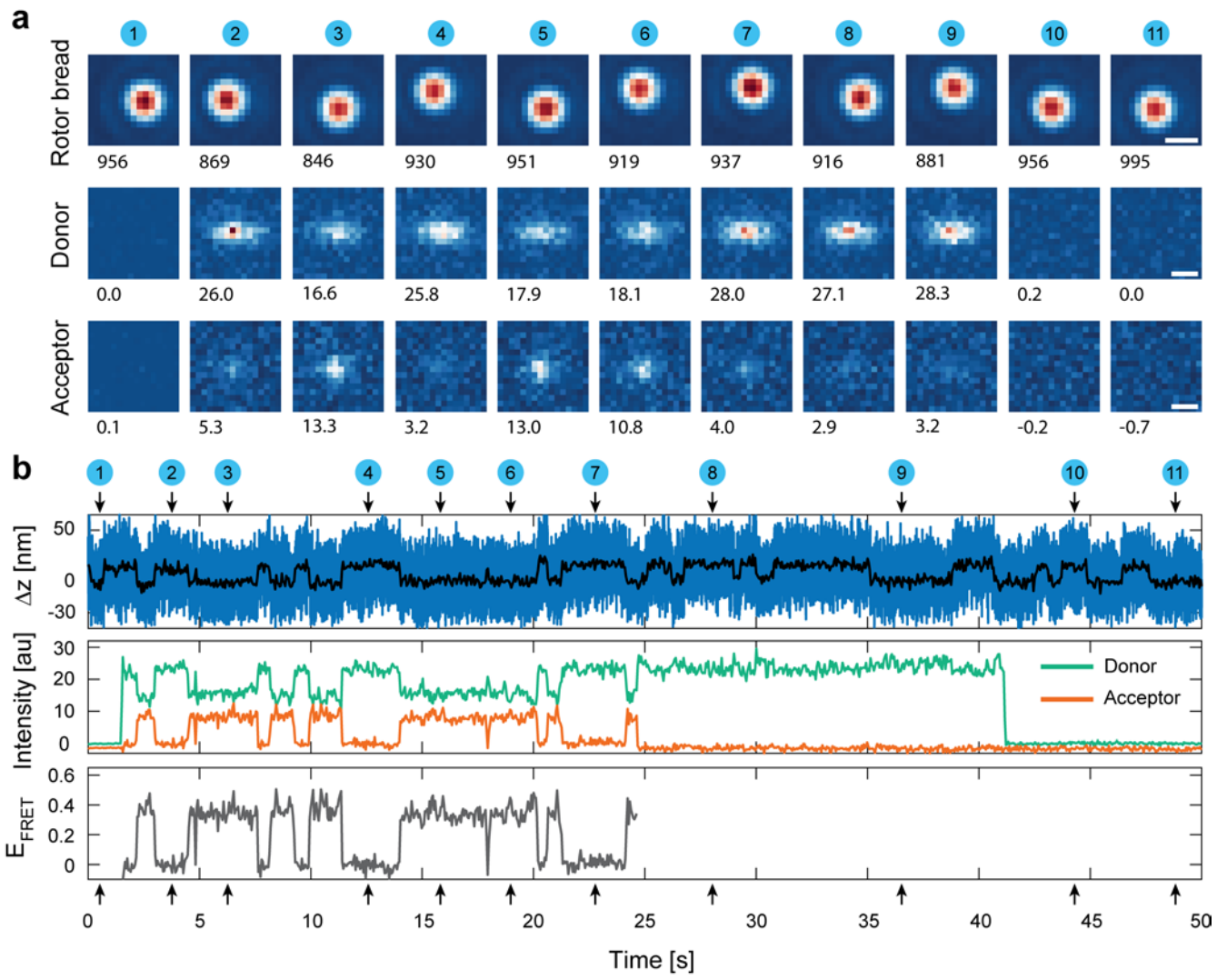

Figure S2. Demonstration of imaging with FluoRBT. (a) Sequence of images of the rotor bead (top) and the donor (middle) and acceptor (bottom) dyes during a FluoRBT experiment. Scale bar: 500 nm. Numbers below the images indicate the measured intensity. The donor and acceptor channels are corrected only for background signal. The donor and acceptor channels are on the same color scale, which is different from the color scale used for images of the rotor bead. Donor bleed into the acceptor channel can be seen in the images, and is corrected before plotting intensities and calculating FRET efficiencies (refer to Methods). We do not detect any signal in the donor and acceptor channels resulting from infrared excitation of the rotor bead and there is correspondingly no crosstalk between Δz and fluorescence intensity channels (see images and traces after both fluorophores have bleached). (b) Measurements of Δz (top), corrected donor and acceptor intensity (middle), and calculated FRET efficiency (bottom) for the full data set. Numbered arrows show the time point for each set of images in (a). See also Movie S1.

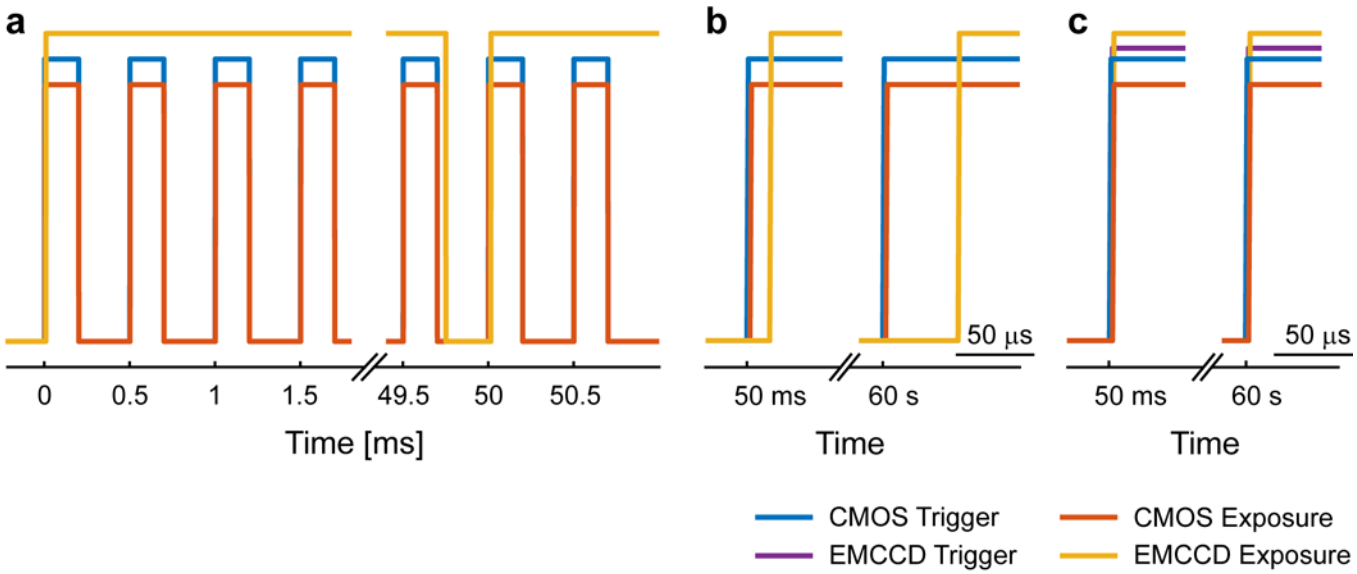

Figure S3. Camera synchronization. Data acquisition from the CMOS camera used for rotor bead tracking and the EMCCD camera used for fluorescence imaging was synchronized via TTL triggers generated by a National Instruments PCIe-6323 card. To validate the camera synchronization, trigger pulses and camera fire outputs (indicating camera exposure) were measured using the PCIe-6323 card at 1 MHz. (a) For experiments reported in this manuscript, exposure of the CMOS camera was initiated at the rising edge of the trigger pulse train and terminated at the falling edge. The EMCCD camera was programmed to start acquisition at the first rising edge of the CMOS trigger pulse train and then continued imaging at a pre-set framerate and exposure time. The CMOS fire output goes to the high state within 1 μs of the trigger signal. The EMCCD fire output goes to the high state 14 μs after the trigger signal. This delay is negligible, even at the highest bandwidth used for comparing fluorescence data to Δz measurements – 100 Hz (Fig. S4b). For this demonstration, microscope cameras were programmed as for hairpin opening experiments, i.e. 2000 Hz imaging of the rotor bead using the CMOS camera and 20 Hz imaging of the fluorophores using the EMCCD camera. (b) Acquisition by the EMCCD camera drifts at ~0.7 μs/s relative to the CMOS camera due to drift between the PCIe-6323 clock and the internal EMCCD camera clock. This leads to delays in exposure up to ~640 μs for the longest traces presented in this manuscript (Figure 2, 890 s); this delay is negligible for these data, as fluorescence is recorded at 5 Hz, and the angular measurements are limited by the rotor bead's rotational relaxation time of ~200 ms. In the traces presented in Figure 3 and Figure S8, there will be ~330 μs delay in exposure between the two cameras by the end of the acquisition, equivalent to ~3% of the 10 ms integration time used for fluorescence exposures and block-averaged extension data. (c) Acquisition by the two cameras can be synchronized to <1 μs using two trigger pulse trains generated by the PCIe-6323 card based on the same master clock. This improved synchronization method was not used for collecting data for this manuscript, but is currently implemented on our instrument and is appropriate for more demanding experiments.

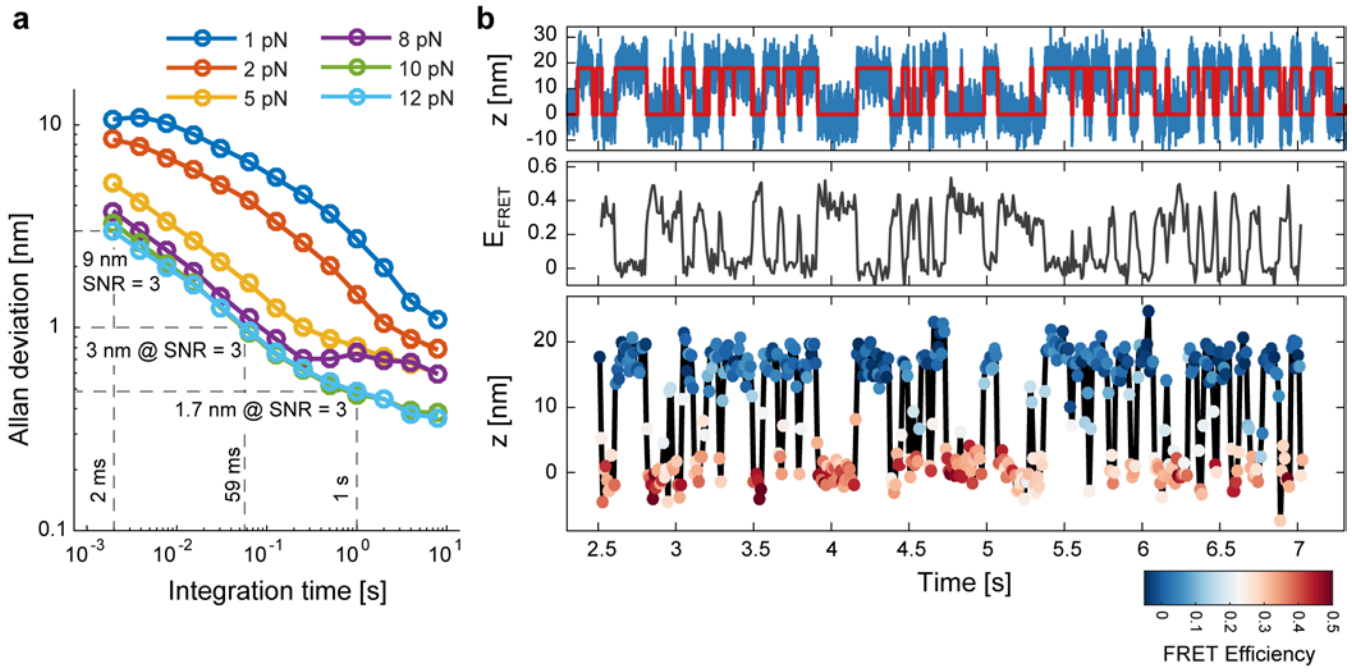

Figure S4. Extension resolution of FluoRBT. (a) The Allan deviation in *Δz* was computed as a function of integration time for a DNA tether with a 300 nm rotor bead ~800 bp away from the surface. The Allan deviation decreases with force due to suppression of axial fluctuations of the bead. Horizontal lines indicate the resolution in *Δz* that can be achieved in the given integration time at high force. Extension noise varies between molecules, and can be lower or higher than seen in panel (a) for individual tethers. For example, the data in Figure 1d show 3-4x higher noise at 50 ms integration time and ~8 pN of tension, and panel (b) here shows a tether with somewhat lower noise. (b) FluoRBT measurements on a 20R25/T4 hairpin tether, highlighting the spatiotemporal resolution achievable with the instrument (Allan deviation of 2.2 nm in 1 ms integration time). Compared with 15R60/T8 (Fig. 1 and Fig. 3), the 20R25/T4 hairpin shows faster transitions between the open and closed states ($\tau_{open} = 67\,ms$ and $\tau_{closed} = 53\,ms$, in agreement with Woodside et al. ($\tau_{1/2} \sim 70\,ms$) (6)). Data were collected at 12 pN in buffer containing 50 mM MOPS pH 7.5, 200 mM KCl, 0.2% Tween-20, 0.2 mg/ml BSA, and 1x oxygen scavenging reagents. Top: Extension data (5000 Hz, blue) allow confident identification of the hairpin state (HMM fit – red). Middle: FRET efficiency of the dye pair (100 Hz) was calculated from the collected donor and acceptor intensities. Bottom: Overlay of FRET efficiency (color scale) and block-averaged *Δz* (100 Hz, black line) shows the correspondence between the two signals.

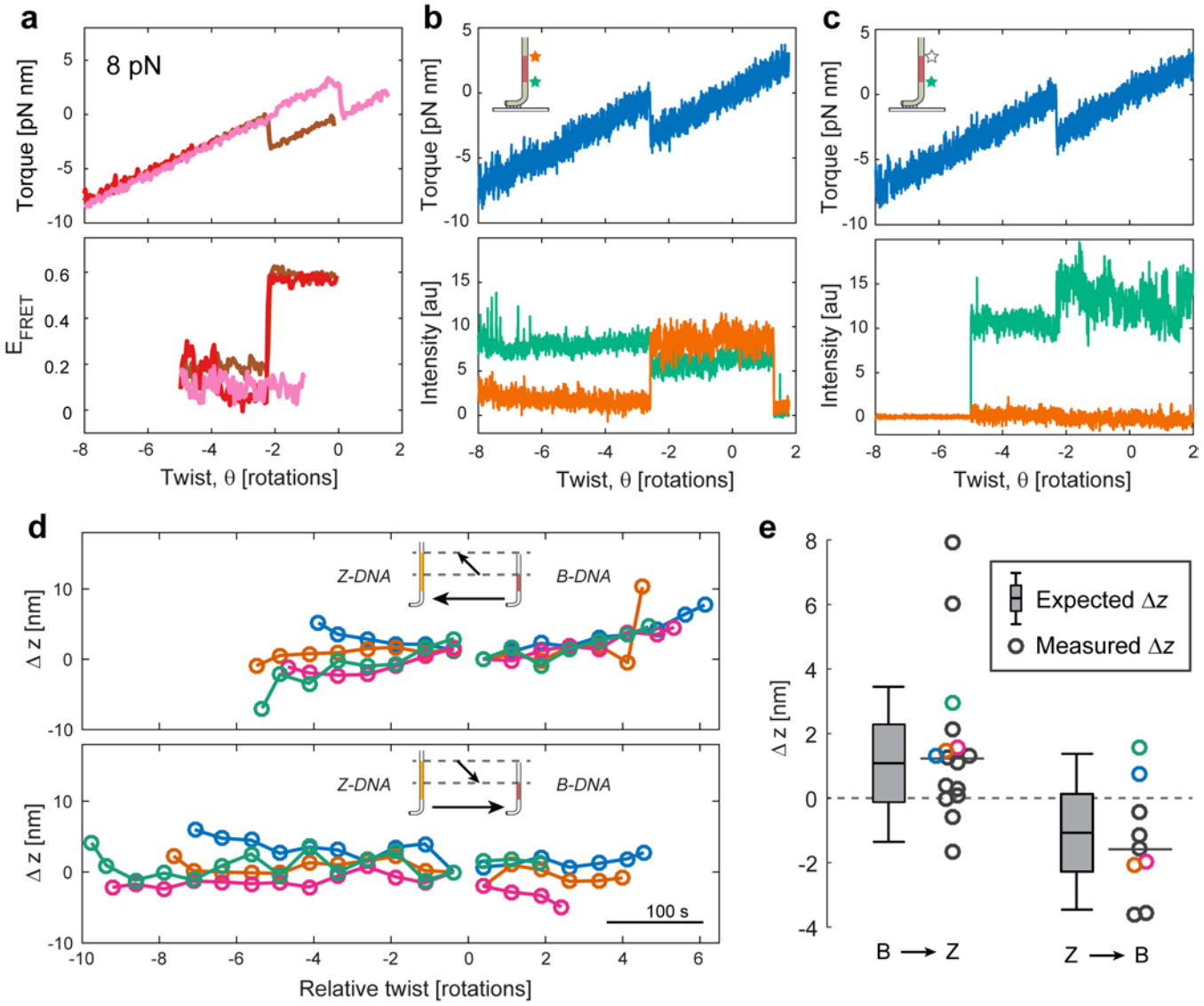

Figure S5. Fluorescence and extension changes at the B-Z transition. (a) FluoRBT measurements on the B-Z structural transition at increased tension (8 pN). Linear fits to the E_{FRET} versus torque data collected under 8 pN and 2 pN (Fig. 2) of tension did not show a significant difference for either B-DNA or Z-DNA state (t-test, $p > 0.3$), although sampling is limited. (b) Donor and acceptor intensities show anticorrelated changes as a function of twist in the molecule, consistent with structural rearrangements in the SOI. At the B-Z transition, we observe a smaller change in donor intensity compared to the change in intensity of the acceptor. Data from this trace are also plotted in blue in Figure 2. (c) In the absence of an acceptor, we observe an increase in donor intensity as the SOI transitions from Z-DNA into B-DNA, in the opposite direction from the intensity change in the presence of a FRET acceptor, and consistent with an environment-dependent change in quantum efficiency of the dye. (d-e) Measuring the change in extension associated with the B-Z transition in the SOI. (d) Changes in extension of the rotor bead as a function of twist during the unwinding (top, SOI transitions from B- to Z-DNA) and rewinding (bottom, SOI transitions from Z- to B-DNA) regions of the torque-twist curve. Low-frequency noise obscures nanometer-scale features over the long timescales of the experiments, but the jump

in extension upon B-Z conversion can be investigated by aligning traces at the B-Z transition. Extension data were block-averaged in 30 s (0.75 rotation) bins starting at the B-Z transition, as detected from the torque channel, and zeroed at the first point before the transition. Data shown are for molecules presented in Figure 2c-d, with matching color. (e) Extension change of the rotor bead as the SOI transitions from B- to Z-DNA (left) and vice versa (right). The 22 base pair SOI is expected to lengthen by ~1 nm as it transitions from B- to Z-DNA (gray box plot, showing expected Δz (band inside of box) ± 1 (top and bottom of box) and ± 2 (whiskers) Allan deviations (1.2 nm) of the data). Colored data points correspond to the first measured Δz after the transition in panel (d). Gray data points are from measurements on other molecules.

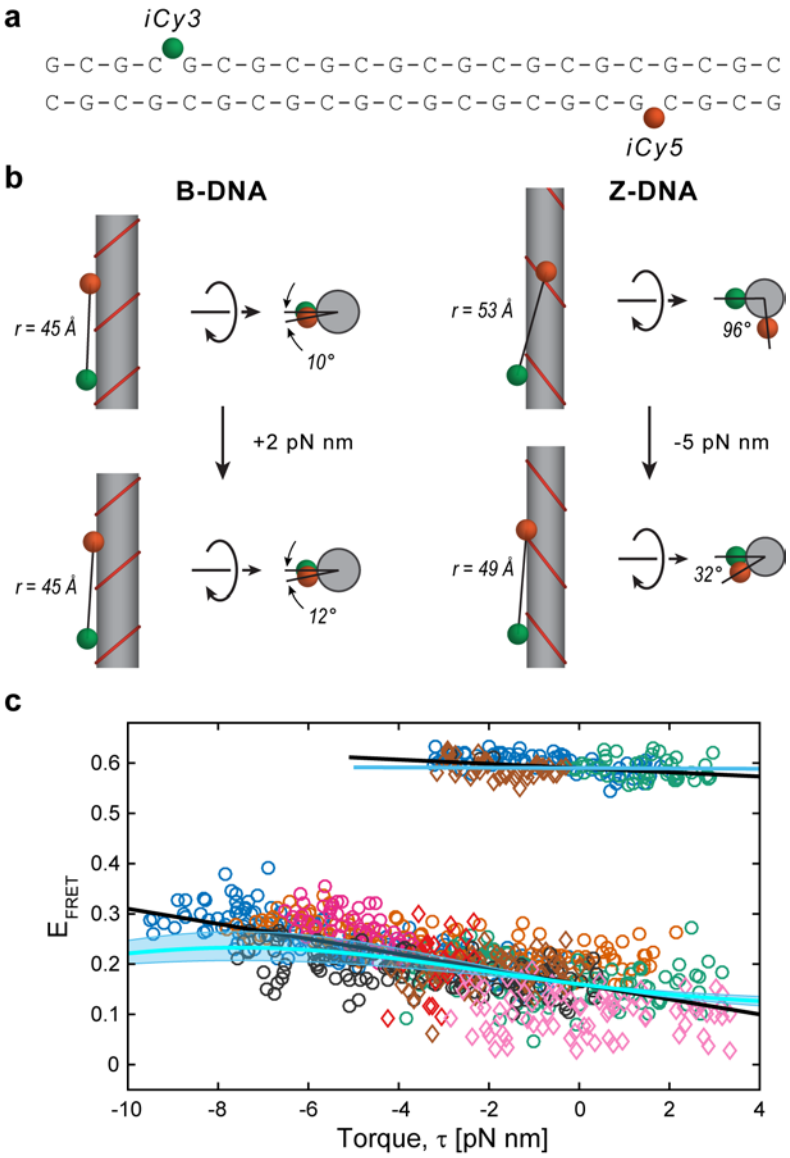

Figure S6. Model for the dependence of dye separation on torque. A complete understanding of the physical basis of the dependence of E_{FRET} on torque awaits detailed experimental and theoretical investigations, including explicit consideration of orientation effects. Here we model the positions of dyes on the duplex, possible changes in dye positions under torque, and resulting FRET changes under simplified assumptions. (a) Schematic of the sequence of interest used in studying the B-Z structural transition. Fluorescent dyes are incorporated into the DNA backbone and likely form bulges on the helix. (b) Top: Dye positions based on molecular modeling (see Methods). The front and top views show the dye separation, *r*, and the angle between the dyes. In B- and Z-DNA the dyes are separated vertically by 44.8 Å and 48.6 Å, respectively. In B-DNA the donor and acceptor are displaced radially from the DNA central axis by 15.0 Å and 14.2 Å, respectively. In Z-DNA, these distances are 13.7 Å and 13.2 Å, respectively. Bottom: Applying torque to the SOI changes the helicity of the segment, leading to changes in dye separation due to rotation of the dye centers around the helix. Z-DNA shows much larger dye displacements because it is torsionally soft in

comparison to B-DNA (1,4,5), and is also modeled under larger absolute torques in the panel shown, reflecting the torque ranges sampled in the experiment. (c) Overlay of E_{FRET} versus torque data for measurements collected at 2 pN of tension (circles, also presented in Figure 2c-d with matching color) and at 8 pN of tension (diamonds, also presented in Figure S5a with matching color). Black lines are linear fits to combined data in B-DNA ($E_{FRET} = -0.0042 * \tau\ [pN\ nm] + 0.59$) and in Z-DNA ($E_{FRET} = -0.015 * \tau\ [pN\ nm] + 0.16$). The obtained zero-torque E_{FRET} values are consistent with ensemble measurements of surface-immobilized partial constructs containing the portion of DNA tether below the SOI (Fig. S7, E_{FRET} = 0.63 ± 0.07 in B-DNA and E_{FRET} = 0.20 ± 0.11 in Z-DNA), and with measurements on a similar construct by Lee et al. (E_{FRET} = 0.50 ± 0.08 in B-DNA and E_{FRET} = 0.12 ± 0.08 in Z-DNA) (8). In Z-DNA E_{FRET} shows larger changes with torque, consistent with the increased torsional compliance of that state. Lee et al. (8) did not report on a change in FRET efficiency with superhelical density (refer to Fig. 4A), possibly due to higher noise in E_{FRET} in their measurement, which also lacked a direct torque measurement. Light blue lines are fits to a simplified model in which E_{FRET} in B- and Z-DNA states changes with torque only as a result of changes in dye separation. For this calculation, R_0 is approximated as fixed (independent of torque) for each state, but is allowed to differ between B-DNA and Z-DNA. R_0 is calculated from the zero-torque E_{FRET} value in (c) using the zero-torque dye separation presented in (b), giving R_0 = 48 Å in B-DNA and R_0 = 40 Å in Z-DNA. The dependence of E_{FRET} on torque is then calculated, using the constant-R_0 approximation in order to gauge expected FRET changes due to probe separation alone. The light blue region around the lines is calculated by adding ± 2.5 Å uncertainty in the radial dye displacement from the helix. The model results suggest that in Z-DNA, the E_{FRET} dependence on torque can be partly explained by changes in dye separation alone. Changes in dipole orientation between the dyes could contribute significantly to changes in E_{FRET} as well. In B-DNA, the dye separation is not expected to change substantially with torque due to the higher torsional rigidity of that state, and the small but measurable FRET changes we observe under torque may depend on orientation effects, or increased compliance introduced by the dyes, or both. Orientation effects, including varying degrees of orientational freedom, could also contribute to the difference in apparent R_0 between the B-DNA and Z-DNA states.

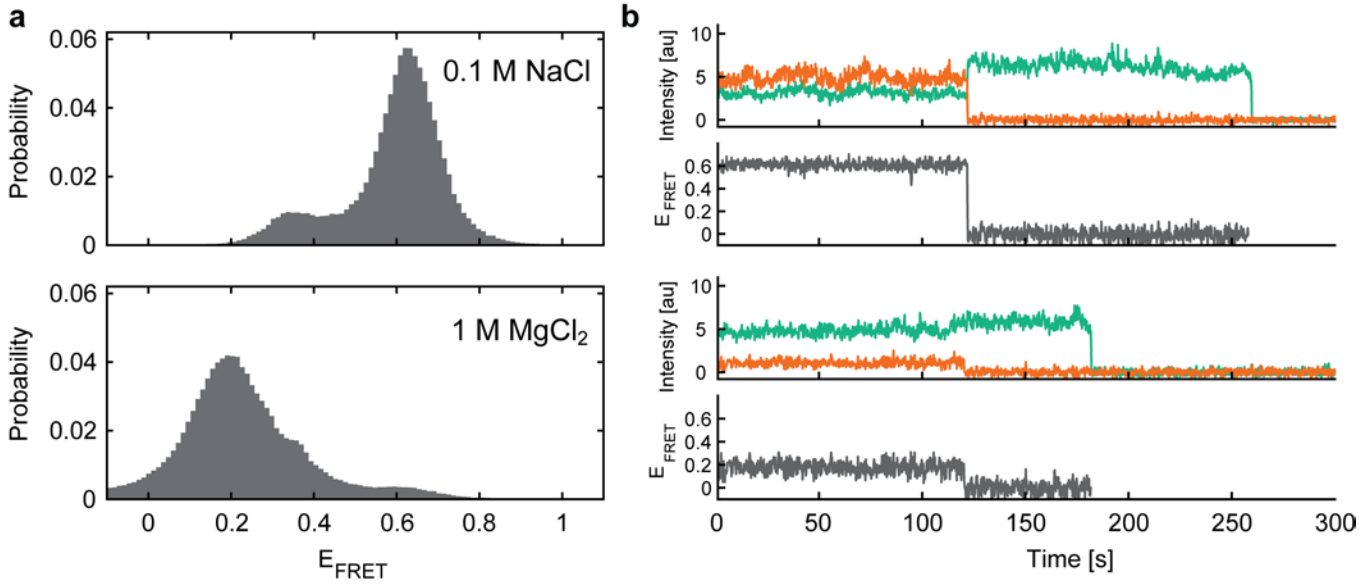

Figure S7. FRET efficiency measurements of the d(pGpC)$_{11}$ sequence of interest immobilized on a surface. Partial constructs containing the GC-repeat were made by annealing and ligating the oligonucleotides MDIG, MDIG-C, F3, F4, GC-1, and GC-2 (see Note 1 and Note 2). Molecules were immobilized on an anti-digoxigenin coated surface and imaged in buffer (40 mM Tris-HCl pH 8.0, 5 mM EDTA, 0.2% Tween-20, 0.01% NaN_3, and 1x oxygen scavenging reagents) containing 0.1 M NaCl (top row) or 1M $MgCl_2$ (bottom row) to favor, respectively, the B-DNA or the Z-DNA state of the SOI. (a) Histograms of instantaneous FRET efficiency measured under conditions favoring the B-DNA (n = 180 molecules, 3.7 min average observation time) or Z-DNA (n = 132 molecules, 3.6 min average observation time) state of the SOI. Only molecules containing a donor and an acceptor dye have been selected for this analysis. Gaussian mixture models were fit to the data to determine the FRET efficiencies of contributing states. Based on the major peak in each condition, the mean FRET efficiency in B-DNA is 0.63 ± 0.07 and in Z-DNA is 0.20 ± 0.11 (mean ± s.d.). The additional peak at E_{FRET} ~ 0.36 is attributed to an intermediate or misfolded state. (b) Example fluorescence intensity and E_{FRET} traces from molecules in B-DNA and Z-DNA state of the SOI. Data are recorded at 5 Hz.

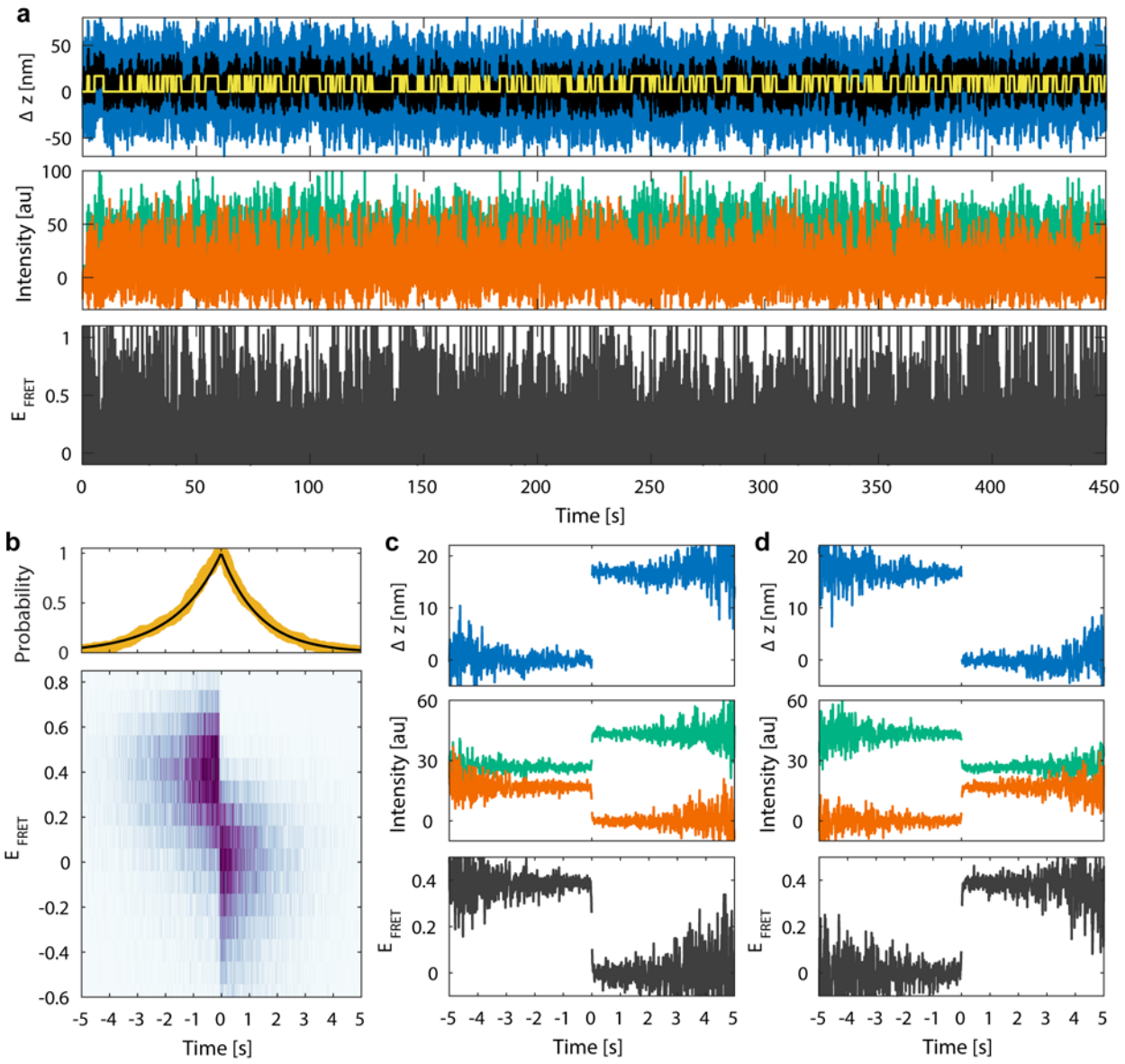

Figure S8. High-resolution FRET measurements via alignment to mechanical data. (a) FluoRBT trace showing many transitions between the open and closed states of a DNA hairpin. This panel is available online as a MATLAB figure file, and excerpts from this trace are also shown in Figure 3a. Top: High-resolution mechanical measurements of ***Δz*** (raw data – blue, and block-averaged – black) allow identification of the hairpin state (HMM fit – yellow) with SNR = 3 in ~10 ms. Middle: Low donor excitation was used to extend the lifetime of the fluorophores, leading to poor SNR in intensity traces (donor – green, and acceptor – orange). Bottom: The calculated instantaneous FRET efficiency shows high measurement noise. (b-d) Data from (a) are excised into pieces containing a single transition of the hairpin (from closed to open state or vice versa) and aligned in time at the transition event. (b) Distribution of hairpin states as a function of time away from the opening event. Top: The probability of state observation (yellow points, based on HMM fit in (a)) decreases exponentially with time (black curves, $\tau_{open} = 1.35\,\mathrm{s}$ and $\tau_{closed} = 1.68\,\mathrm{s}$) on timescales close to a previous

study using this hairpin ($\tau_{1/2} = 1.3\ s$) (7). Bottom: Post-synchronized histogram of instantaneous FRET measurements. (c-d) Averaging of time-aligned traces reduces uncorrelated noise and provides high-resolution FRET measurements for each state. Data were aligned to (c) opening or (d) closing events. Fluorescence intensity changes can be detected with SNR ~1 in the raw data (a) and with SNR ~13 in the post-synchronized data (c-d).

Note 1. Building blocks for DNA tethers.

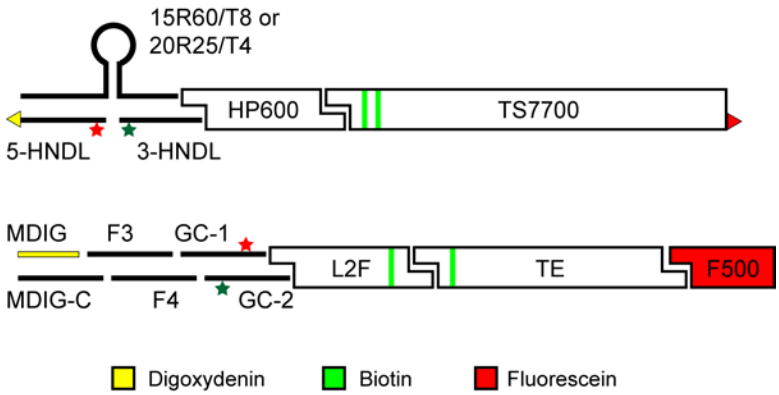

The schematic above depicts the building blocks used for DNA tether construction. PCR templates, primers, and restriction enzymes used for construction of linear DNA pieces are given in Table S1. Synthetic oligonucleotides used in making of the DNA hairpins and the $d(pGpC)_{11}$ sequence of interest are given in Table S2. DNA modifications used for attaching the tether to the surface, the magnetic bead, or the rotor bead are color-coded (yellow – digoxigenin, green — biotin, red — fluorescein); terminal modifications are indicated by angle brackets (< for 5' and > for 3' modification). Also, /5Phos/: 5' phosphorylation, /idSp/: 1',2'-Dideoxyribose spacer, /Q570-dT/: Quasar 570 C6 dT, /Q670-dT/: Quasar 670 C6 dT, /iCy3/: internal Cy3 modification, /iCy5/: internal Cy5 modification. Oligonucleotides were purchased from Integrated DNA Technologies, ATDBio, or Alpha DNA. 15R60/T8 and 20R25/T4 were designed based on hairpin sequences reported in Ref. (6) and Ref. (7). GC-1 and GC-2 were designed based on sequences used in Ref. (8).

Table S1. PCR templates, primers, and restriction enzymes used for tether construction.

	Primers	Length	Template	Digest
TS7700	ttgcgaagaccagattCTTCCTTTCGGCTGAGGTTAATCAC <TACTGTTGATGGGTGTCTGGTC	7763	pLC-M6-898-IQ12	BbsI
HP600	gatcgaagacacaatcGCCGTGGATGTGCGACGTATTC ctaagaagactactaaAACGACGGCCAGTGCCAAG	638	pMS-SGS1	BbsI
F500	gatcgaagacacttagACAACCCACAAGTATAGAGGCTCCTATG GACGCGGATATAATGACATTTCCTAAC	520	pFO-SE1	BbsI
TE	gaagggtctcagattTCACTATAGGGCGAATTGGAGCTCC gaagggtctcactaaCACTAAAGGGAACAAAAGCTGGGTAC	4156	pFO-SE2	BsaI
L2F	gatcgaagacacaatcAAGTATGCGCCGCTACAGGGC gatcgaagacagtgacATACCGCTCGCCGCAGC	691	pBSII_SK	BbsI

Table S2. DNA oligonucleotides used for tether construction.

	Sequence
3-HNDL	/5Phos/TTAGGTGCACG/Q570-dT/AGCT
5-HNDL	TC/Q670-dT/CCATTTTCCTATTACCGGTGCCACGC>
15R60/T8	GCGTGGCACCGGTAATAGGAAAATGGAGA/idSp/GAGTCCTGGATCCTGTTTTTTTTCAGGAT CCAGGACTC/idSp/AGCTACGTGCAC
20R25/T4	GCGTGGCACCGGTAATAGGAAAATGGAGA/idSp/AAGTTAACATCTAGATTCTATTTTTAGAAT CTAGATGTTAACTT/idSp/AGCTACGTGCAC
GC-1	/5Phos/ACTGCTGGTACGCGCGCGCGCGCGCGCG/iCy5/CGCGATCGAC
GC-2	/5Phos/GTCAGTCGATCGCGCGCGCGCGCGCGCG/iCy3/CGCGTACCAG
MDIG	<GGAAGGAGATTCTCGACAGTTCTAATTGACCTCTTACCTTTTCCCAGTTCAATCTTTGTCAAA CACC
MDIG-C	/5Phos/GGCCATGGTGTTTGACAAAGATTGAACTGGGAAAAGGTAAGAGGTCAATTAGAACTG TCGAGAATCTCCTTCC
F3	/5Phos/ATGGCCGGGATGCATGGGTTCAACTGC
F4	/5Phos/CAGTGCAGTTGAACCCATGCATCCC

Note 2. List of parts. Essential components for adding fluorescence excitation and emission detection paths to the evanescent scattering rotor bead tracking instrument described in Ref. (1). Optical filters were selected for the specific combination of dyes and light sources used in the experiments outlined in the main text. Optics mounting hardware was purchased from Thorlabs, Inc.

- CMOS camera (Mikrotron EoSens CL)
- EMCCD camera (Andor iXon+ 897)
- 532 nm laser (Spectra-Physics Excelsior single-mode, 100 mW)
- 633 nm laser (Melles Griot 25-LHP-925-249, 20 mW)
- Microscope objective (Nikon 60x Apo TIRF, NA 1.49)
- Fiber launch system (Olympus PlanN 10x objective, Thorlabs P1-630PM-FC-2 optical fiber, Thorlabs MBT613D mechanical stage)
- Shutters (nmLaser LST200SLP) with home-built controllers
- Collimator, C1 (Thorlabs F280FC-A)
- Polarizing beam splitter, PBS (Thorlabs PBS121)
- Zero-order quarter wave plate, QWP (Thorlabs WPQ05M-532)
- Lenses, L1 and L2 (Thorlabs A397TM-A and AC254-050-A-ML)
- Lens, L3 (Thorlabs AC254-500-A-ML)
- Mirrors, M1-3 (Thorlabs BB1-E02)
- Coupling mirrors, CM1-2 (Edmund Optics 54-092)
- Iris, I1 (Thorlabs SM1D12C)
- 532 nm notch filter, F1 (Chroma NF03-532E-25)
- 633 nm notch filter, F2 (Chroma NF02-633S-25)
- 755 nm dichroic beamsplitter, DBS2 (Semrock FF775-Di01-25x36)
- 550 nm long-pass filter, F3 (Chroma HHQ550LP)
- 842 nm short-pass filter, F4 (Semrock FF01-842/SP-25)
- 200 mm tube lens, IL1 (Thorlabs ITL200)
- 650 nm dichroic beamsplitter, DBS3 (Semrock FF650-Di01-25x36)
- Lens, L4 (Ø25 mm, f ~ 2000 mm)
- Beam splitter, BS1 (Thorlabs BST11R)
- Lens, L5 (Ø25 mm, f = 1000 mm)
- 2.5x magnifying relay lenses (Nikon)
- Optical splitters, OS1 and OS2 (Cairn Research, OptoSplit II and OptoSplit III)

Mirror M4 and imaging lens IL2 are part of the Nikon Eclipse Ti-S microscope body on which the instrument is built. Unlike Ref. (1), in this work we used a blue fiber-coupled LED (Thorlabs M470F1) for observation of magnetic beads.

References

1. Lebel, P., A. Basu, F. C. Oberstrass, E. M. Tretter, and Z. Bryant. 2014. Gold rotor bead tracking for high-speed measurements of DNA twist, torque and extension. Nat. Methods 11:456-462.

2. Nishizaka, T., Y. Hasimoto, and T. Masaike. 2011. Simultaneous Observation of Chemomechanical Coupling of a Molecular Motor. In Single Molecule Enzymology: Methods and Protocols. G. I. Mashanov andC. Batters, editors. Humana Press. Totowa, NJ. 259-271.

3. Kalinin, S., T. Peulen, S. Sindbert, P. J. Rothwell, S. Berger, T. Restle, R. S. Goody, H. Gohlke, and C. A. M. Seidel. 2012. A toolkit and benchmark study for FRET-restrained high-precision structural modeling. Nat. Methods 9:1218-1225.

4. Oberstrass, F. C., L. E. Fernandes, and Z. Bryant. 2012. Torque measurements reveal sequence-specific cooperative transitions in supercoiled DNA. Proc. Natl. Acad. Sci. U.S.A. 109:6106-6111.

5. Oberstrass, F. C., L. E. Fernandes, P. Lebel, and Z. Bryant. 2013. Torque spectroscopy of DNA: base-pair stability, boundary effects, backbending, and breathing dynamics. Phys. Rev. Lett. 110:178103.

6. Woodside, M. T., W. M. Behnke-Parks, K. Larizadeh, K. Travers, D. Herschlag, and S. M. Block. 2006. Nanomechanical measurements of the sequence-dependent folding landscapes of single nucleic acid hairpins. Proc. Natl. Acad. Sci. U.S.A. 103:6190-6195.

7. Long, X., J. W. Parks, C. R. Bagshaw, and M. D. Stone. 2013. Mechanical unfolding of human telomere G-quadruplex DNA probed by integrated fluorescence and magnetic tweezers spectroscopy. Nucleic Acids Res. 41:2746-2755.

8. Lee, M., S. H. Kim, and S. C. Hong. 2010. Minute negative superhelicity is sufficient to induce the B-Z transition in the presence of low tension. Proc. Natl. Acad. Sci. U.S.A. 107:4985-4990.

9. Sarkar, A., R. B. Robertson, and J. M. Fernandez. 2004. Simultaneous atomic force microscope and fluorescence measurements of protein unfolding using a calibrated evanescent wave. Proc. Natl. Acad. Sci. U.S.A. 101:12882-12886.

10. Watanabe, T. M., T. Sato, K. Gonda, and H. Higuchi. 2007. Three-dimensional nanometry of vesicle transport in living cells using dual-focus imaging optics. Biochem. Biophys. Res. Commun. 359:1-7.

11. Milescu, L. S., C. Nicolai, and J. Bannen. 2000-2013. QuB Software.

12. Roy, R., S. Hohng, and T. Ha. 2008. A practical guide to single-molecule FRET. Nat. Methods 5:507-516.

13. Huguet, J. M., C. V. Bizarro, N. Forns, S. B. Smith, C. Bustamante, and F. Ritort. 2010. Single-molecule derivation of salt dependent base-pair free energies in DNA. Proc. Natl. Acad. Sci. U.S.A. 107:15431-15436.

14. Zheng, G., X.-J. Lu, and W. K. Olson. 2009. Web 3DNA—a web server for the analysis, reconstruction, and visualization of three-dimensional nucleic-acid structures. Nucleic Acids Res. 37:W240-W246.

15. Stein, I. H., V. Schüller, P. Böhm, P. Tinnefeld, and T. Liedl. 2011. Single-Molecule FRET Ruler Based on Rigid DNA Origami Blocks. ChemPhysChem 12:689-695.

16. Woźniak, A. K., G. F. Schröder, H. Grubmüller, C. A. M. Seidel, and F. Oesterhelt. 2008. Single-molecule FRET measures bends and kinks in DNA. Proc. Natl. Acad. Sci. U.S.A. 105:18337-18342.

17. Choi, U. B., P. Strop, M. Vrljic, S. Chu, A. T. Brunger, and K. R. Weninger. 2010. Single-molecule FRET-derived model of the synaptotagmin 1-SNARE fusion complex. Nat. Struct. Mol. Biol. 17:318-324.